

# Evidence for a change in the radiation mechanism in the hard state of GRO J1655–40. Hysteresis in the broad-band noise components

P. Reig<sup>1,2\*</sup>, I.E. Papadakis<sup>2,1</sup>, M.A. Sobolewska<sup>3</sup>, J. Malzac<sup>4,5</sup>

<sup>1</sup>IESL, Foundation for Research and Technology, 71110 Heraklion, Crete, Greece

<sup>2</sup>Department of Physics and Institute of Theoretical & Computational Physics, University of Crete, PO Box 2208, GR-710 03, Heraklion, Crete, Greece

<sup>3</sup>Harvard-Smithsonian Center for Astrophysics, 60, Garden Street, Cambridge, MA 02138, USA

<sup>4</sup>Université de Toulouse; UPS-OMP; IRAP; Toulouse, France,

<sup>5</sup>CNRS; IRAP; 9 Av. colonel Roche, BP 44346, F-31028 Toulouse cedex 4, France

Accepted ??, Received ??; in original form ??

## ABSTRACT

We have analysed archival data from the *Rossi X-ray Timing Explorer (RXTE)* to study the aperiodic variability of the black-hole binary GRO J1655–40 during the hard state of the 2005 outburst. This work was motivated by the recent finding of a spectral change in the hard state X-ray radiation mechanism in black hole binaries. We computed the 0.008–64 Hz power spectral density during the rise and decay of the 2005 outburst, and we found that they were reasonably well modelled by the sum of two, broad Lorentzian functions in most cases (plus a narrow QPO) which correspond to three different variability components. Our aim is to study the evolution of the timing properties of the source during the outburst, by studying the correlation between the characteristics of the broad-band noise components in the power spectra and the source luminosity. Our results suggest that the whole power spectrum shifts to high (low) frequencies as the source luminosity increases (decreases), in agreement with previous studies of other black hole binaries. However, we also detect a strong “hysteresis” pattern in the “frequency-luminosity” plots, and show that the “critical” luminosity limit, above which the timing properties of the source change, is different during the rise and the decay phase of the outburst. We discuss the general implications of these results in the context of the truncated disc model.

**Key words:** accretion, accretion discs – black hole physics – X-rays: binaries

## 1 INTRODUCTION

Black-hole binaries (BHBs) consist of a black hole orbiting a “normal” companion. By “normal” it is meant that nuclear burning in its interior is still the main source of energy. BHBs divide up into low-mass and high-mass systems. Although the two first BHBs discovered, namely Cyg X–1 (Webster & Murdin 1972) and LMC X–3 (Cowley et al. 1983) were persistent high-mass BHBs, low-mass transient BHB represent the vast majority of BHBs. They are strong sources of high-energy radiation and show a richness in their X-ray variability properties. High-mass BHB tend to be persistent sources, while low-mass BHBs are normally transient sources containing a Roche lobe overflowing M-A star. Transient BHBs exhibit X-ray outbursts lasting for a few weeks (Remillard & McClintock 2006). During these outbursts the X-ray luminosity increases by several orders of magnitude from a quiescent level of  $10^{-6} - 10^{-8} L_{\text{Edd}}$  (Gallo et al. 2008) to a peak level of  $\sim L_{\text{Edd}}$ , where  $L_{\text{Edd}}$  is the Eddington luminosity ( $L_{\text{Edd}} \approx 1.3 \times 10^{38} (M/M_{\odot}) \text{ erg cm}^{-2} \text{ s}^{-1}$ ,

for a black hole of mass  $M$ ). Thus low-mass BHBs are also called “X-ray novae”.

Hard X-rays in BHBs are thought to be produced in the vicinity of the black hole, in the region between the event horizon and the inner parts of the accretion disc. The main emission mechanisms that are currently believed to produce the X-rays in the 2–100 keV band are Compton up-scattering and blackbody radiation. The spectrum from the accretion disc is the sum of blackbody components, with increasing temperature and luminosity, as the disc radius decreases. Typically, the temperature in the innermost part of the disc is 0.1–0.3 keV. These low-energy photons emitted by the disc gain energy by means of inverse Compton in a region around the black hole that is generally called as the “corona”, generating a continuum spectrum with a power-law shape which extends up to a few hundred keV. The formation and heating mechanism, as well as the geometry, of the corona is one of the unsolved issues in black-hole binary physics. The corona could even be the base of a mildly relativistic radio jet (Markoff et al. 2005). Alternatively, the hard X-rays detected in the hard state could be generated by

\* E-mail: pau@physics.uoc.gr

**Table 1.** Summary of the RXTE observations.

Proposal ID	MJD	On-source time (ks)
P90058	53424.01–53431.17	15.2
P90428	53426.04–53432.79	83.5
P90704	53439.74–53439.61	6.3
P91404	53433.90–53436.40	17.1
P91702	53436.72–53660.97	212.2
P91704	53637.17–53637.50	19.8

inverse Comptonization in the jet itself (see e.g. Kylafis et al. 2008, and references therein).

The monitoring of the evolution of the X-ray spectral and timing parameters over the course of an outburst reveals significant changes in their spectral and timing properties. Although these properties change smoothly as the outburst progresses, most of the phenomenology is better understood by invoking two main source states: a “hard” and a “soft” state<sup>1</sup>. The relative contribution of the above mentioned mechanisms can broadly explain the spectral properties of the sources in the two states: whenever the accretion disc dominates, the power-law continuum is soft, and a broad, thermal, blackbody-like spectrum is also observed; if emission from the corona dominates, then only the Comptonised power-law “tail” shows up in the spectrum (with slopes which are flatter than those detected in the soft state). The hard state generally appears at the beginning and end of the outbursts, while the soft state is observed at the peak of the outburst.

GRO J1655–40 is one of the best studied BHBs. It is one of the most firmly established black hole candidates and its astrophysical parameters are fairly well known. GRO J1655–40 was discovered by BATSE onboard the Compton Gamma Ray Observatory in July 1994 (Zhang et al. 1994). It is located at a distance of  $3.2 \pm 0.2$  kpc (Hjellming & Rupen 1995, but see Foellmi et al. 2006) and contains a black hole with a mass of  $6.3 \pm 0.3 M_{\odot}$  (Remillard & McClintock 2006) and spin  $a = 0.78 \pm 0.10$  (Gierlinski et al. 2001). The optical counterpart is an F3 IV-F6 IV star with a mass of  $2.3 M_{\odot}$  in a 2.6 day orbit. The inner disk is viewed at an inclination of  $70^{\circ}$  (Orosz & Bailyn 1997).

Past timing studies of GRO J1655–40 have focused mainly on the properties of quasi-periodic oscillations (QPO) that are detected in its power spectral density (PSDs). Shaposhnikov et al (2007) analysed data from the early stages of the 2005 outburst and found that the low-frequency QPO strongly correlates with the spectral parameters. They concluded that the region where the QPO originates moves inward as the outburst progressed. The correlation between spectral and timing parameters can also be used to estimate the mass of the black hole (Shaposhnikov & Titarchuk 2009). The smooth day-to-day variation of the QPO frequency during the 2005 outburst led Chakrabarti et al. (2008) to suggest that an oscillating shock, which sweeps inward through the disk in the rising phase and outward in declining phase, is responsible for the QPO. The explanation of the shock oscillations was preferred to that one that assumes that QPO are generated by orbiting blobs at the inner edge of the accretion disk because the QPO is a stable and lasting feature,

<sup>1</sup> For a detailed classification of black-hole states and state transitions see e.g. Belloni (2010).

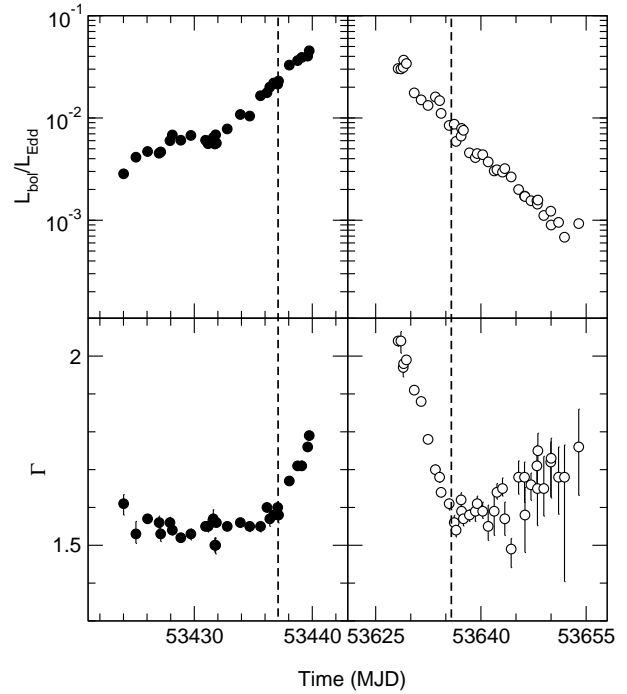


**Figure 1.** X-ray luminosity (upper panel) and power-law photon index (lower panel) as a function of time. Filled and opened symbols represent the rise and decay of the outburst, respectively. The vertical dashed lines indicate the time of the first (left) and last (right) appearance of  $L_0$  (see Sect. 3.1).

which has to survive for weeks (Debnath et al. 2008). Motta et al. (2012) made a detailed analysis of the QPOs in GRO J1655–40 under the *ABC* classification scheme (see e.g. Casella et al. 2005). These authors reported the *simultaneous* detection of type-B and type C QPO during the peak of the outbursts, in the so-called ultra-luminous state, indicating that these two types of QPO gave a different physical origin. Motta et al. (2012) also studied the properties of the peaked noise component detected in the ultra-luminous state.

Recently, Sobolewska et al. (2011, S11 hereafter, see also Wu & Gu 2008) performed an X-ray *spectral* analysis and found that the “power-law spectral index – luminosity” relation of GRO J1655–40 (and GX 339–4) changes when the source luminosity is greater than  $L_{crit,S11} = 0.006 \pm 0.002$  of the Eddington limit. Motivated by this result, we studied in this work the broad-band noise components that dominate the X-ray aperiodic variability of GRO J1655–40, using *RXTE* data collected during the 2005 outburst of the source. We are mainly interested in investigating the variation of their parameters with the source’s luminosity and spectral shape, with the hope that this X-ray *timing* analysis may shed light on the X-ray source geometry, the accretion mode as well as the radiation mechanisms that operate when the source is in the hard state.

## 2 OBSERVATIONS AND DATA ANALYSIS

### 2.1 The *RXTE* observations

We analysed *RXTE* data of GRO J1655–40 during the 2005 outburst. Since we wish to investigate fast time X-ray variability ( $\sim 0.1$ –100 s) we only used data from the Proportional Counter (PCA). The PCA consists of five Proportional Counter Units (PCUs) with a to-

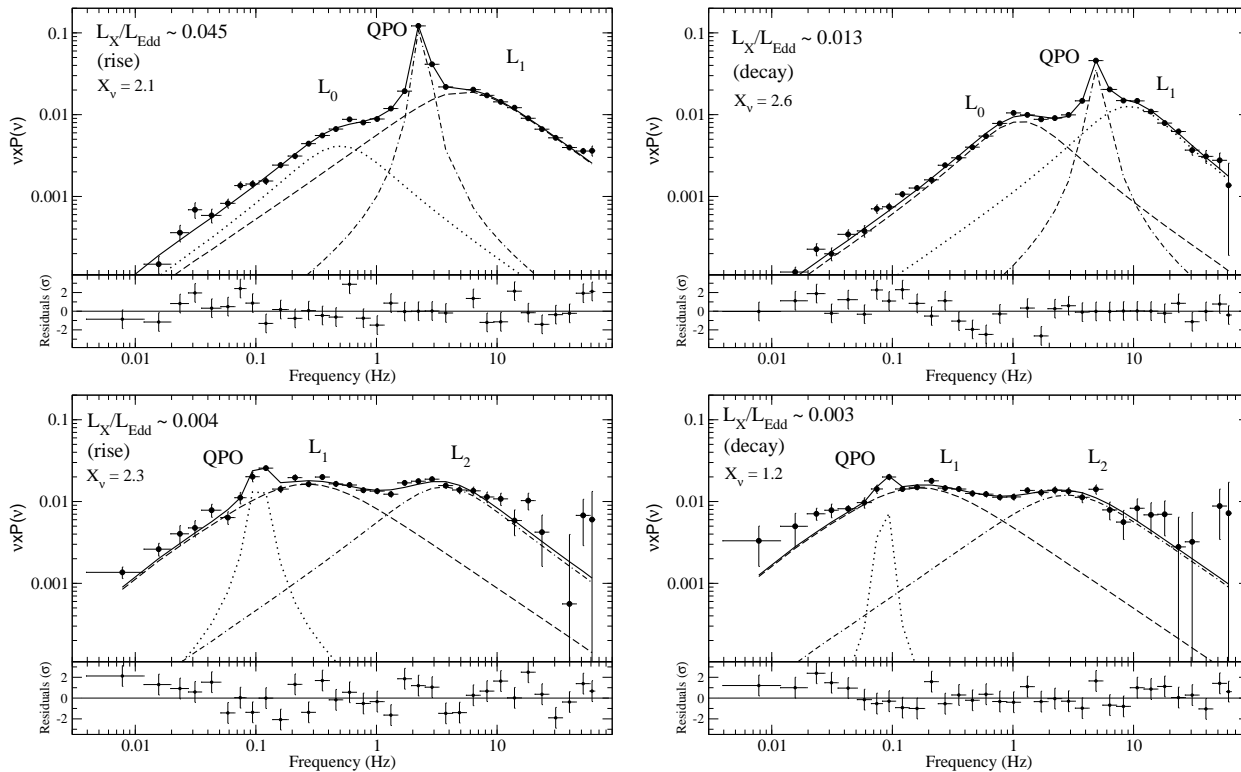


**Figure 2.** Representative power spectra of GRO J1655–40 during the rise and decay phases of the outburst.

tal collecting area of  $\sim 6250$  cm<sup>2</sup>. It operates in the 2–60 keV range and has a nominal energy resolution of 18% at 6 keV (Jahoda et al. 1996). The data were retrieved from the *RXTE* archived and correspond to the observation programs given in Table 1.

We selected the data with the same criteria as in S11, namely, we discarded all observations with a photon index of  $\Gamma \gtrsim 2$ . The source was in the canonical hard state in all observations of the rise phase of the outburst. The decay phase include hard-intermediate and hard state observations (Motta et al. 2012). The photon index values resulted from the best fit to the PCA+HEXTE 3–200 keV spectra as described in Sobolewska et al. (2009). We only considered the *RXTE* data up to MJD 53654, which include light curves with an average count rate larger than 22.5 counts s<sup>-1</sup> in the 2–13 keV band, because the PSD estimation is less reliable at lower count rates. The total number of observations which satisfy this criterion are 69, representing a total on-source exposure time of 326 ks.

Fig. 1 shows the X-ray luminosity (from 0.01 to 1000 keV) in Eddington units, plotted as a function of time (on MJD) for the selected *RXTE* observations. Because the majority of energy in BHBS is radiated in the X-ray band, we consider the X-ray luminosity to be representative of the bolometric flux, hence we denote with ' $L_{\text{bol}}/L_{\text{Edd}}$ ' the ratio of the X-ray luminosity to the Eddington limit. We used the  $L_{\text{bol}}/L_{\text{Edd}}$  values of S11, which were based on the best, DISKBB + EQPAIR model fits to the spectra of the source (see S11 for details). The upper panel in Fig. 1 indicates that the data we use in this work cover well the rise and the decay of the 2005 X-ray outburst of GRO J1655–40. In the bottom panel of the same figure we plot  $\Gamma$  as a function of time. This plot indicates the spectral evolution of the source during the rising and decaying phases of the outburst, which was studied in detail by S11.

## 2.2 Computation and fitting of the power spectra

Power spectra (PSD) were computed using PCA data in the energy range 2–13 keV. Light curves with a time resolution of  $2^{-7}$  s were divided into 128-s segments and a Fast Fourier Transform was computed for each segment. Thus the frequency range sampled by the power spectra was 0.008–64 Hz. The final power spectrum was computed as the average of all power spectra obtained for each segment. These averaged power spectra were logarithmically rebinned in frequency and corrected for dead time effects according to the prescriptions given in Nowak et al. (1999). Power spectra were normalized in a way that the integral is equal to the squared fractional rms amplitude, according to the so-called rms-normalization.

Usually, models that include Lorentzian profiles fit well the broad-band PSD of BHBS in their hard state (Belloni et al. 2002; Pottschmidt et al. 2003; Axelsson et al. 2005). We therefore constructed a conservative model with as few Lorentzian profiles as possible, to fit the PSDs in our sample. The Lorentzian functions are characterized by their normalization,  $R$  (which determines the total rms amplitude of the Lorentzian), their resonance frequency,  $\nu_c$ , and its quality factor,  $Q$ , which is defined as  $Q = \nu/\text{FWHM}$  ( $\text{FWHM}$  is the full frequency width of the Lorentzian at half of its maximum value). Traditionally, profiles with  $Q > 2$  are referred to as “narrow” and are indicative of quasi-periodic oscillations. On the other hand, profiles with  $Q < 2$  are known as peaked noise and correspond to “broad-band” components in the PSDs. Instead of  $\nu_c$ , we used the peak frequency of the Lorentzian (i.e. the frequency where the contribution of the Lorentzian to the total rms is maximized), which is defined as  $\nu_{\text{max}} = (\nu_c^2 + (\text{FWHM}/2)^2)^{1/2}$  in the  $\nu \times P_\nu$  representation of the PSD. All the Lorentzian parameters were left free to vary during the fitting procedure.

We found that most of the PSDs were well fitted by the sum

**Table 2.** Best-fit parameters of the  $L_0$ ,  $L_1$  and  $L_2$  components for the rise phase of the outburst.

MJD	$L_{\text{bol}}/L_{\text{Edd}}$	RMS (%) (0.01-10Hz)	$Q_0$	$\nu_0$ (Hz)	$rms_0$	$Q_1$	$\nu_1$ (Hz)	$rms_1$	$Q_2$	$\nu_2$	$rms_2$	$\chi_r^2$
53424.009	0.0028	30.4	—	—	—	0.10	0.094 <sup>+0.029</sup> <sub>-0.008</sub>	0.307 <sup>+0.039</sup> <sub>-0.025</sub>	0.00	2.485 <sup>+0.593</sup> <sub>-0.587</sub>	0.300 <sup>+0.022</sup> <sub>-0.124</sub>	1.30
53425.055	0.0041	30.5	—	—	—	0.00	0.147 <sup>+0.023</sup> <sub>-0.012</sub>	0.311 <sup>+0.072</sup> <sub>-0.020</sub>	0.00	2.540 <sup>+0.701</sup> <sub>-0.691</sub>	0.298 <sup>+0.011</sup> <sub>-0.011</sub>	2.08
53426.040	0.0047	30.6	—	—	—	0.03	0.149 <sup>+0.009</sup> <sub>-0.008</sub>	0.313 <sup>+0.006</sup> <sub>-0.004</sub>	0.00	3.070 <sup>+0.213</sup> <sub>-0.202</sub>	0.319 <sup>+0.005</sup> <sub>-0.005</sub>	1.46
53427.022	0.0045	29.8	—	—	—	0.00	0.264 <sup>+0.021</sup> <sub>-0.024</sub>	0.321 <sup>+0.008</sup> <sub>-0.009</sub>	0.26	3.596 <sup>+0.513</sup> <sub>-0.448</sub>	0.241 <sup>+0.010</sup> <sub>-0.006</sub>	2.35
53427.155	0.0047	28.9	—	—	—	0.00	0.242 <sup>+0.020</sup> <sub>-0.015</sub>	0.316 <sup>+0.007</sup> <sub>-0.018</sub>	0.25	3.851 <sup>+0.317</sup> <sub>-0.306</sub>	0.244 <sup>+0.011</sup> <sub>-0.006</sub>	1.30
53427.942	0.0060	29.5	—	—	—	0.05	0.231 <sup>+0.015</sup> <sub>-0.016</sub>	0.307 <sup>+0.007</sup> <sub>-0.007</sub>	0.12	3.697 <sup>+0.297</sup> <sub>-0.219</sub>	0.274 <sup>+0.006</sup> <sub>-0.005</sub>	1.28
53428.138	0.0068	29.5	—	—	—	0.01	0.186 <sup>+0.018</sup> <sub>-0.013</sub>	0.311 <sup>+0.013</sup> <sub>-0.032</sub>	0.11	3.012 <sup>+0.267</sup> <sub>-0.273</sub>	0.278 <sup>+0.058</sup> <sub>-0.019</sub>	0.88
53428.859	0.0061	29.8	—	—	—	0.00	0.226 <sup>+0.010</sup> <sub>-0.009</sub>	0.335 <sup>+0.005</sup> <sub>-0.009</sub>	0.19	3.722 <sup>+0.182</sup> <sub>-0.173</sub>	0.255 <sup>+0.022</sup> <sub>-0.012</sub>	1.46
53429.712	0.0067	29.4	—	—	—	0.00	0.271 <sup>+0.025</sup> <sub>-0.022</sub>	0.330 <sup>+0.004</sup> <sub>-0.005</sub>	0.21	3.878 <sup>+0.315</sup> <sub>-0.340</sub>	0.245 <sup>+0.016</sup> <sub>-0.010</sub>	1.52
53430.958	0.0061	30.2	—	—	—	0.05	0.171 <sup>+0.015</sup> <sub>-0.018</sub>	0.327 <sup>+0.024</sup> <sub>-0.009</sub>	0.00	3.220 <sup>+3.610</sup> <sub>-0.432</sub>	0.297 <sup>+0.010</sup> <sub>-0.011</sub>	1.18
53431.173	0.0056	27.8	—	—	—	0.00	0.176 <sup>+0.013</sup> <sub>-0.015</sub>	0.291 <sup>+0.009</sup> <sub>-0.013</sub>	0.02	3.067 <sup>+0.123</sup> <sub>-0.005</sub>	0.283 <sup>+0.011</sup> <sub>-0.008</sub>	1.98
53431.612	0.0064	29.1	—	—	—	0.00	0.288 <sup>+0.027</sup> <sub>-0.021</sub>	0.288 <sup>+0.009</sup> <sub>-0.009</sub>	0.15	3.945 <sup>+0.447</sup> <sub>-0.406</sub>	0.255 <sup>+0.009</sup> <sub>-0.036</sub>	1.49
53431.743	0.0056	29.1	—	—	—	0.00	0.229 <sup>+0.041</sup> <sub>-0.030</sub>	0.314 <sup>+0.006</sup> <sub>-0.008</sub>	0.16	3.543 <sup>+0.329</sup> <sub>-0.312</sub>	0.259 <sup>+0.026</sup> <sub>-0.005</sub>	2.31
53431.810	0.0068	28.1	—	—	—	0.09	0.298 <sup>+0.054</sup> <sub>-0.051</sub>	0.287 <sup>+0.008</sup> <sub>-0.028</sub>	0.17	4.011 <sup>+0.706</sup> <sub>-0.706</sub>	0.249 <sup>+0.053</sup> <sub>-0.032</sub>	1.89
53431.875	0.0057	29.0	—	—	—	0.00	0.241 <sup>+0.022</sup> <sub>-0.024</sub>	0.319 <sup>+0.004</sup> <sub>-0.007</sub>	0.16	4.101 <sup>+0.361</sup> <sub>-0.384</sub>	0.258 <sup>+0.007</sup> <sub>-0.017</sub>	2.41
53432.793	0.0078	29.2	—	—	—	0.00	0.329 <sup>+0.019</sup> <sub>-0.019</sub>	0.338 <sup>+0.004</sup> <sub>-0.007</sub>	0.29	4.617 <sup>+0.439</sup> <sub>-0.468</sub>	0.226 <sup>+0.014</sup> <sub>-0.017</sub>	2.69
53433.905	0.0108	28.4	—	—	—	0.00	0.510 <sup>+0.018</sup> <sub>-0.020</sub>	0.335 <sup>+0.004</sup> <sub>-0.004</sub>	0.23	5.764 <sup>+0.388</sup> <sub>-0.312</sub>	0.223 <sup>+0.003</sup> <sub>-0.003</sub>	1.21
53434.694	0.0104	28.4	—	—	—	0.00	0.645 <sup>+0.046</sup> <sub>-0.048</sub>	0.329 <sup>+0.006</sup> <sub>-0.008</sub>	0.00	6.250 <sup>+0.835</sup> <sub>-0.700</sub>	0.261 <sup>+0.008</sup> <sub>-0.022</sub>	2.53
53435.612	0.0165	28.3	—	—	—	0.06	0.795 <sup>+0.073</sup> <sub>-0.076</sub>	0.336 <sup>+0.005</sup> <sub>-0.013</sub>	0.18	8.469 <sup>+1.211</sup> <sub>-0.334</sub>	0.205 <sup>+0.028</sup> <sub>-0.053</sub>	1.16
53436.159	0.0177	28.9	—	—	—	0.10	0.749 <sup>+0.076</sup> <sub>-0.029</sub>	0.311 <sup>+0.013</sup> <sub>-0.005</sub>	0.10	6.874 <sup>+0.324</sup> <sub>-0.324</sub>	0.243 <sup>+0.004</sup> <sub>-0.004</sub>	2.46
53436.398	0.0200	29.0	—	—	—	0.00	1.045 <sup>+0.055</sup> <sub>-0.052</sub>	0.362 <sup>+0.006</sup> <sub>-0.017</sub>	0.36	10.247 <sup>+1.060</sup> <sub>-1.193</sub>	0.174 <sup>+0.021</sup> <sub>-0.006</sub>	3.59
53436.725	0.0220	29.3	—	—	—	0.01	1.055 <sup>+0.052</sup> <sub>-0.061</sub>	0.358 <sup>+0.003</sup> <sub>-0.005</sub>	0.22	9.356 <sup>+0.713</sup> <sub>-0.763</sub>	0.196 <sup>+0.019</sup> <sub>-0.003</sub>	2.21
53437.072	0.0214	29.5	—	—	—	0.05	1.050 <sup>+0.079</sup> <sub>-0.079</sub>	0.345 <sup>+0.018</sup> <sub>-0.018</sub>	0.31	9.371 <sup>+0.929</sup> <sub>-1.043</sub>	0.187 <sup>+0.022</sup> <sub>-0.024</sub>	2.66
53437.142	0.0230	30.3	0.00	0.012 <sup>+0.064</sup> <sub>-0.025</sub>	0.113 <sup>+0.110</sup> <sub>-0.039</sub>	0.12	1.140 <sup>+0.176</sup> <sub>-0.102</sub>	0.330 <sup>+0.023</sup> <sub>-0.080</sub>	0.26	10.121 <sup>+1.638</sup> <sub>-1.587</sub>	0.193 <sup>+0.024</sup> <sub>-0.019</sub>	2.25
53438.054	0.0329	30.0	0.21	0.289 <sup>+0.108</sup> <sub>-0.085</sub>	0.139 <sup>+0.046</sup> <sub>-0.031</sub>	0.41	1.978 <sup>+0.189</sup> <sub>-0.219</sub>	0.32 <sup>+0.030</sup> <sub>-0.019</sub>	0.00	10.477 <sup>+3.713</sup> <sub>-2.273</sub>	0.227 <sup>+0.013</sup> <sub>-0.021</sub>	1.30
53438.757	0.0364	30.6	0.67	0.301 <sup>+0.020</sup> <sub>-0.024</sub>	0.094 <sup>+0.004</sup> <sub>-0.004</sub>	0.00	3.335 <sup>+0.120</sup> <sub>-0.090</sub>	0.359 <sup>+0.000</sup> <sub>-0.000</sub>	—	—	—	2.44
53439.107	0.0390	30.7	0.75	0.313 <sup>+0.031</sup> <sub>-0.033</sub>	0.081 <sup>+0.005</sup> <sub>-0.006</sub>	0.04	3.385 <sup>+0.067</sup> <sub>-0.061</sub>	0.366 <sup>+0.023</sup> <sub>-0.002</sub>	—	—	—	3.11
53439.610	0.0402	30.4	0.52	0.372 <sup>+0.037</sup> <sub>-0.030</sub>	0.098 <sup>+0.005</sup> <sub>-0.003</sub>	0.14	4.130 <sup>+0.051</sup> <sub>-0.105</sub>	0.330 <sup>+0.002</sup> <sub>-0.002</sub>	—	—	—	3.53
53439.741	0.0453	29.5	0.38	0.498 <sup>+0.058</sup> <sub>-0.054</sub>	0.114 <sup>+0.011</sup> <sub>-0.010</sub>	0.15	5.265 <sup>+0.210</sup> <sub>-0.213</sub>	0.301 <sup>+0.012</sup> <sub>-0.011</sub>	—	—	—	2.09

of three Lorentzians. One of them was “narrow” and corresponds to the QPO feature that has been studied in the past. The other two turned out to be “broad”. As we argue in the next section, our results indicate that the broad Lorentzian components correspond to *three* different types of noise, that we shall refer to as  $L_i$  with  $i = 0, 1, 2$ . Only two PSDs (those which correspond to the observations taken on MJD=53437.1417 and 53438.0537) are best fitted by a model which includes the three broad Lorentzian components, that is, the three types of noise (plus the QPO). In all other PSDs,  $L_0$  and  $L_2$  do not appear together. In five observations (MJD 53628–53629) only one component (plus the QPO) was enough to fit the PSD.

Figure 2 shows four representative power spectra at low and high luminosity for the rising and decaying phases of the outburst. The plots of the power spectra are shown in the  $\nu \times P_\nu$  representation, where each power is multiplied by the corresponding frequency (Belloni et al. 2002).

In Tables 2 and 3 we list the best-fit values of the Q-parameter ( $Q_i$ ), maximum frequency ( $\nu_i$ ), and the fractional amplitude of variability  $rms_i$  (normalisation of the Lorentzian), for each one of the  $L_0$ ,  $L_1$ , and  $L_2$  broad Lorentzian components. Also listed is the overall RMS, estimated by the integral of the overall PSD over the observed frequency range. Note that Tables 2 and 3 do not include the  $L_{\text{QPO}}$  best-fit parameter values.

The best-fit  $\chi_r^2$  indicate that the quality of the fit is not statistically acceptable in quite a few cases. The residuals do not always imply a good fit due to the presence of statistically significant

“wiggles” in the data. In some cases, these wiggles are indicative of sharp features, and in other cases of weaker and broader features. However, we did not attempt to model further these features, as our aim is not to provide the best possible description to the PSDs of the source, but rather to provide a reliable characterization of the broad PSD shape at all luminosities and investigate its evolution. As the plots of the “bad fit quality” PSDs in Fig. 2 show, even in this case, two main Lorentzian profiles, plus the QPO, can describe accurately the main characteristics of the broad band noise components in the PSD of the source.

### 3 PSD MODEL FITTING RESULTS

#### 3.1 The evolution of the Lorentzian peak frequencies and rms amplitude

The time evolution of the best-fit  $L_i$  peak frequencies and rms during the rise (filled symbols) and decay phase (open symbols) of the outburst is shown on the top and bottom panels of Fig. 3, respectively. The star-like symbols in the right panels (decay) represent the hard-intermediate state observations. At the beginning of the outburst, the PSDs are well described by the sum of two Lorentzians, whose peak frequencies increase with the source luminosity (left top panel of Fig. 3). We denote with  $L_1$  and  $L_2$  the lower and higher frequency Lorentzians, respectively. The dashed line indicates the time at which a third Lorentzian appears in the



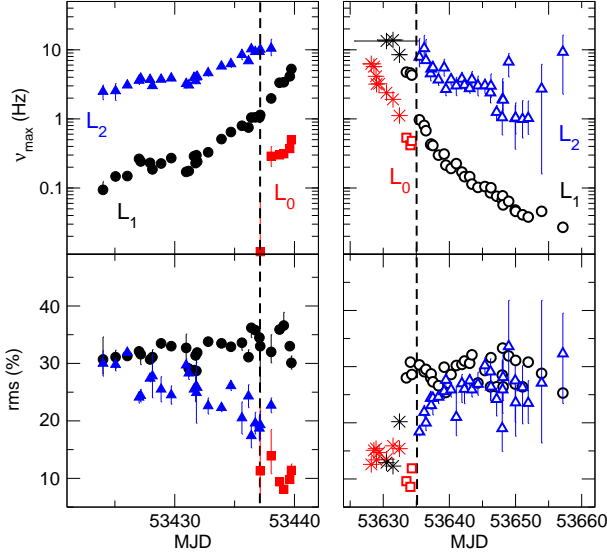


**Figure 3.** Time evolution of the peak frequency and rms amplitude (top and bottom panel, respectively) of the noise components during the rise and decay phases of the outburst (left and right panel, respectively). Red squares, black circles and blue triangles indicate the  $L_0$ ,  $L_1$ , and  $L_2$  best-fit parameter values, while filled (open) symbols correspond to the rise (decay) parts of the outburst. Stars represent the hard-intermediate state observations. The vertical dashed lines indicate the time of the first (left) and last (right) appearance of  $L_0$ , which corresponds to a luminosity of 0.03 and 0.01  $L_{\text{Edd}}$ , respectively.

It remains constant at a level of  $\sim 10$ – $15\%$  during both the rise and decay phase of the outburst. The higher values of  $\text{rms}_0$  correspond to the hard-intermediate state.

Our results indicate that  $L_0$  is a broad Lorentzian ( $Q \lesssim 0.7$ ), which peaks in the range of 0.1–6 Hz. It is only detected in 6 out of 29 PSDs during the rise (when  $L > 0.03L_{\text{Edd}}$ ) and 11 out of 41 PSDs during the decay (when  $L > 0.01L_{\text{Edd}}$ ).  $L_1$  is almost always present, except for the first five PSDs during the decay phase of the outburst, when the source flux is high, and  $\text{rms}_1 < 10\%$ . Its characteristic frequency varies in the range 0.05–10 Hz. This component is consistent with being a zero-centred Lorentzian ( $Q \sim 0$ ) in most PSDs.  $L_2$  is detected only when  $L < 0.03L_{\text{Edd}}$ , in the rise phase, and  $L < 0.01L_{\text{Edd}}$ , during the decay.  $Q_2$  is always smaller than  $\sim 0.3$ , and most of the time is consistent with zero.

The top panel in Fig. 4 shows the “ $v_{\text{max},0}$  vs  $v_{\text{max},1}$ ” and “ $v_{\text{max},2}$  vs  $v_{\text{max},1}$ ” plots (squares and triangles, respectively; filled and open symbols indicate the rise and decay phase of the outburst). Clearly, the peak frequencies evolve in a highly correlated way during the outburst. We fitted both data sets in the top panel of Fig. 4 with a power law model. The solid and dashed lines in this panel indicate the best-fit results to the “ $v_{\text{max},2}$  vs  $v_{\text{max},1}$ ” and “ $v_{\text{max},0}$  vs  $v_{\text{max},1}$ ” data sets, respectively. The fit was done in the log-log space, using the `fitxy` subroutine of Press et al. (1992), which takes into account the errors on both variables (we assumed that the  $v_{\text{max}}$  errors are symmetric and equal to the mean of the best-fit positive and negative confidence limits listed in Table 2). The best-fit results are as follows:  $\log(v_{\text{max},2}) = 0.94(\pm 0.02) + 0.58(\pm 0.03)\log(v_{\text{max},1})$  ( $\chi^2 = 46.8$  for 53 degrees of freedom - dof) and  $\log(v_{\text{max},0}) = -1.21(\pm 0.07) + 1.3(\pm 0.1)\log(v_{\text{max},1})$  ( $\chi^2 = 6.1$  for 9 dof). The best fit results indicate that the peak frequencies do not increase (or decrease) with the same rate. The  $v_{\text{max},2} \propto v_{\text{max},1}^{0.6}$  and  $v_{\text{max},0} \propto v_{\text{max},1}^{1.3}$

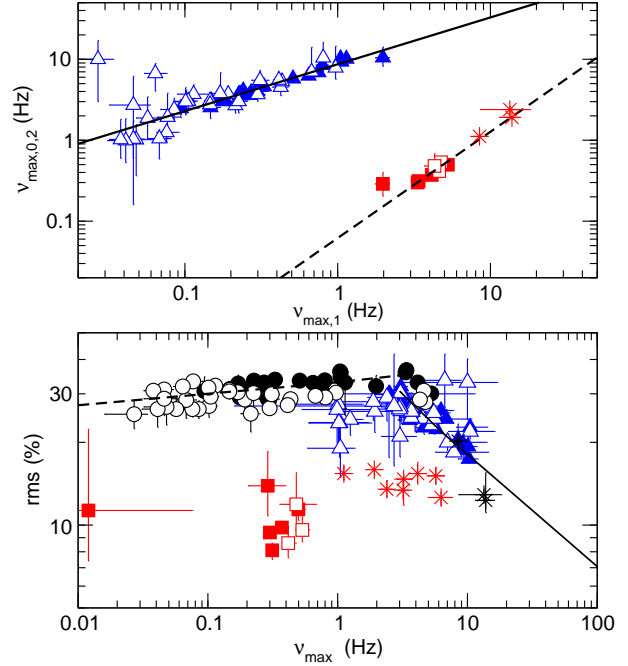


**Figure 4.** Top panel: the  $L_0$  and  $L_2$  peak frequencies plotted as a function of  $v_{\text{max},1}$  (squares and triangles, respectively) and best-fit lines. Bottom panel: the Lorentzian rms plotted as a function of the respective peak frequencies (red squares, black circles and blue triangles for the  $L_0$ ,  $L_1$  and  $L_2$  components, respectively). Filled and open symbols indicate the rise and decay parts of the outburst in both panels. Stars represent the hard-intermediate state observations. The dashed line represents the best fit to the  $L_1$  points below 1 Hz, while the solid line fits the  $L_2$  points above 3 Hz.

relations suggest that  $v_{\text{max},1}$  evolves faster than  $v_{\text{max},2}$  and slower than  $v_{\text{max},0}$ , during the rise and decay phases of the outburst.

The bottom panel in Fig. 4 shows the “rms vs peak frequency” plots for the three Lorentzians. We observe a bimodal behaviour in the case of  $L_1$  and  $L_2$ . At low characteristic frequencies,  $\text{rms}_1$  increases slowly with increasing frequency, until  $v_{\text{max},1} \sim 1$ – $3$  Hz. The dashed line in the same panel indicates the best fit linear model to the  $(\text{rms}_1, v_{\text{max},1})$  data (in the log-log space) when  $v_{\text{max}} < 1$  Hz. The best-fit results indicate that a relation of the form:  $\text{rms}_1 \propto v_{\text{max},1}^{0.042 \pm 0.005}$ , fits the data reasonably well. Although the slope is shallow, it is nevertheless significantly different from zero. This relation appears to fit the data well up to  $v_{\text{max},1} \sim 3$  Hz. At higher frequencies,  $\text{rms}_1$  anti-correlates with  $v_{\text{max},1}$ , both for the rise and the decay data. This behaviour is also seen in Cyg X–1 (Pottschmidt et al. 2003; Axelsson et al. 2005, see also Klein-Wolt & van der Klis 2008).

We observe a similar behaviour between  $\text{rms}_2$  and  $v_{\text{max},2}$ . The solid line in the bottom panel of Fig. 4 indicates the best-fit line to all the  $(\text{rms}_2, v_{\text{max},2})$  data at frequencies greater than 3 Hz. The results indicate that the best-fit relation of the form:  $\text{rms}_2 \propto v_{\text{max},2}^{-0.41 \pm 0.03}$  describes well the “ $\text{rms}_2$  –  $v_{\text{max},2}$ ” anti-correlation at frequencies above 3 Hz. At lower frequencies, there may be a positive correlation between  $\text{rms}_2$  and  $v_{\text{max},2}$ , (as is the case with  $L_1$ ) but the number of data points is not large enough to draw a positive conclusion.

On the contrary,  $\text{rms}_0$  is roughly constant at around  $\sim 10$ – $15\%$ , irrespective of the source flux. Perhaps it is slightly higher during the decay phase, but the  $L_0$  data points in the bottom panel of Fig. 4 do not suggest any correlation between  $\text{rms}_0$  and  $v_{\text{max},0}$ .

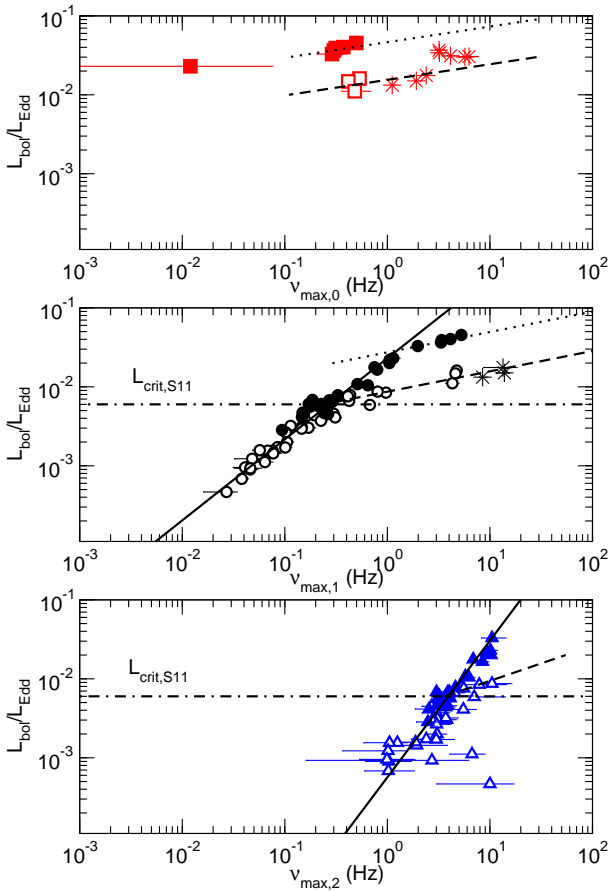


**Figure 5.** The “peak frequency–luminosity” relation for  $L_0$ ,  $L_1$  and  $L_2$  (top, middle and lower panels, respectively). Filled and open symbols indicate the data sets for the rise and decay outburst phase, respectively. Stars (decay) represent the hard-intermediate state observations. The horizontal dot-dashed line in the middle and bottom panels indicates the critical luminosity level of S11,  $L_{crit,S11}$ .

### 3.2 The “peak frequency – luminosity” relation

Given the Lorentzian peak frequencies ( $\nu_{max}$ ) evolution during the outburst (shown in Fig. 3), we expect that  $\nu_{max}$  will correlate with the source flux as well. Fig. 5 shows the relation between  $\nu_{max}$  and  $L_{bol}/L_{Edd}$ . In these plots, we chose to plot  $L_{bol}/L_{Edd}$  in the  $y$ -axis, similar to the “hardness–intensity” diagrams that are frequently used in the study of the spectral evolution of the outbursts in BHs. Clearly, the frequencies correlate positively with source flux. Since the peak Lorentzian frequencies are also well correlated with each other (see Fig. 4), it appears that the whole PSD shifts to higher frequencies with increasing flux, and then shifts back to lower frequencies, as the flux decreases.

A hysteresis effect is clearly seen in the  $L_0$  and  $L_1$  plots. In the case of  $L_0$  (upper panel in Fig. 5), at a given luminosity the peak frequencies during the decay phase (open symbols) are systematically higher than the respective frequencies during the rise phase of the outburst (filled symbols). The same effect is observed in the case of  $L_1$  (middle panel in Fig. 5). When the source luminosity is greater than  $L_{crit,S11}$  (this “critical” luminosity level is indicated by the horizontal dot-dashed line in the middle panel of Fig. 5) the “ $\nu_{max,1} - L_{bol}/L_{Edd}$ ” relation during the decay phase of the outburst is different from the “peak frequency – luminosity” in the rise phase. As a result,  $\nu_{max,1,decay}$  is always greater than  $\nu_{max,1,rise}$  when

$L_{bol}/L_{Edd} > L_{crit,S11}$ . At lower luminosities, the “ $\nu_{max,1} - L_{bol}/L_{Edd}$ ” relation is very similar for both the rise and the decay data sets.

During the decay phase, the characteristic frequency of  $L_1$  displays a gap between 1 and 3 Hz (middle panel of Fig. 5). This gap corresponds to the “jump” that appears in the  $\nu_{max,1}$  evolution when  $L_0$  disappears and  $L_2$  appears (upper right panel in Fig. 3). It is interesting to note that a similar discontinuity has been reported for the QPO frequency in GRO J1655–40 and GX 339–4 only during the decline phase of an outburst (but not during the rise phase) with no corresponding discontinuity in the count rate (Chakrabarti et al. 2008; Nandi et al. 2012).

To quantify the relation between  $\nu_{max,1}$  and  $L_{bol}/L_{Edd}$ , we first fitted the (rise and decay) data below  $L_{crit,S11}$  with a linear function (in the log-log space) of the form:  $\log(\nu_{max,1}) = a_1 + \beta_1 \times \log(L_{bol}/L_{Edd})$ . The best-fit parameter values are:  $\beta_1 = 0.98 \pm 0.04$  and  $a_1 = 1.6 \pm 0.1$ . The solid line in the middle panel of Fig. 5 indicates the best-fit model to the data. Strictly speaking, the best-fit model is not statistically accepted ( $\chi^2 = 187$  for 33 dof). However, as Fig. 5 shows, the best fit line describes rather well the “ $\nu_{max,1} - L_{bol}/L_{Edd}$ ” relation at luminosities lower than  $L_{crit,S11}$ . In fact, this relation appears to also fit well the  $[\nu_{max,1}, (L_{bol}/L_{Edd})]$  data in the rise phase up to  $L \sim 0.03L_{Edd}$ . At this luminosity level,  $\nu_{max,1} \sim 2$  Hz. According to the “ $rms_1 - \nu_{max,1}$ ” relation plotted in the bottom panel of Fig 4, at higher frequencies (and hence luminosities)  $rms_1$  starts to decrease.

The dashed line in the same panel indicates the best-fit of the same linear model to the  $[\log(\nu_{max,1}), \log(L_{bol}/L_{Edd})]$  data during the decay phase, when the source luminosity is greater than  $L_{crit,S11}$ . The best fit results are:  $\beta_1 = 3.9 \pm 0.2$  and  $a_1 = 8.0 \pm 0.4$  ( $\chi^2 = 73.5$  for 10 dof). Interestingly, the same model line (with the normalization increased by a factor of  $\sim 3$ ) represents well the “ $\nu_{max,1} - L_{bol}/L_{Edd}$ ” relation during the rise phase, when the source luminosity is larger than  $0.03 L_{Edd}$  (dotted line in the middle panel of Fig. 5; note that this line does not indicate a best-fit model, but is a copy of the dashed line in the same panel, shifted by a factor of 3 along the  $y$ -axis). Therefore, the  $L_1$  properties (i.e.  $rms$  and the dependence of  $\nu_{max,1}$  on source luminosity), change above  $0.03 L_{Edd}$  in the rise phase of the outburst.

The “ $\nu_{max,2} - luminosity$ ” relation (bottom panel in Fig. 5) appears to be roughly similar for both the rise and the decay phases of the outburst. The horizontal dot-dashed line in the same panel indicates  $L_{crit,S11}$ , at which point  $\nu_{max,2} \sim 3$  Hz. As we discussed in the previous section, at higher frequencies (and hence luminosities),  $rms_2$  starts decreasing.

Since  $L_1$  is present in almost all observations, and hence provides a detailed picture of the relation between peak frequency and luminosity, we used the best-fit “ $\nu_{max,2} - \nu_{max,1}$ ” relation (from section 3.1) and the best-fit “ $\nu_{max,1} - luminosity$ ” relation, and found that  $\nu_{max,2} \propto L^{0.57}$  for luminosities below  $L_{crit,S11}$  in the rise phase, while  $\nu_{max,2} \propto L^{2.3}$  when the source luminosity is greater than  $L_{crit,S11}$  in the decay phase. The two relations are indicated by the solid and dashed lines in the bottom panel of Fig. 5, respectively. The solid line agrees well with the  $[\nu_{max,2}, (L_{bol}/L_{Edd})]$  data in the rise phase, all the way up to the highest luminosity at which  $L_2$  is detected. Regarding the decay phase,  $L_2$  is detected in a few PSDs when the source luminosity is greater than  $L_{crit,S11}$ . Nevertheless, the few available points agree with the dashed line. This suggests that the  $L_2$  “peak frequency – luminosity” relation above  $L_{crit,S11}$  may not be the same during the rise and decay phases, assuming that  $L_2$  still operates even in the cases when we cannot detect it.

During the decay phase,  $L_2$  is not detected until  $L_{bol}/L_{Edd}$  decreases below  $0.01L_{Edd}$ , while during the rise phase, we cannot

detect  $L_2$  when the source luminosity is larger than  $\sim 0.03L_{\text{Edd}}$ . In both cases,  $\nu_{\text{max},2} \sim 10\text{Hz}$ , and  $\text{rms}_2 \sim 10\%$ . In fact, the “ $\nu_{\text{max},2}$ –rms” anti-correlation (shown in the bottom panel of Fig. 4) indicates that the  $L_2$  rms should keep decreasing at higher luminosities. The combination of these two facts (increasing peak frequency above 10 Hz, and decreasing rms below 10%, as the luminosity increases) suggests that  $L_2$  may be always present, but cannot be detected because it becomes too weak and shifts to frequencies too high to be detected in the present PSDs, especially so if  $L_2$  were affected by a similar frequency discontinuity to that seen in  $L_1$  at MJD 53635 (dashed line in Fig. 3).

In order to quantify the  $L_0$  “peak frequency – luminosity” relation, we found that  $\nu_{\text{max},0} \propto L^{5.1}$  according to the best-fit “ $\nu_{\text{max},0} - \nu_{\text{max},1}$ ” relation (section 3.1) and the best-fit “ $\nu_{\text{max},1} - \text{luminosity}$ ” relation in the decay phase above  $L_{\text{crit},S11}$ . This relation is indicated by the dashed line in the top panel of Fig. 5. The line agrees reasonably well with the data in the decay phase (except perhaps during the highest luminosity phase, when only  $L_0$  is detected in the PSD). The dotted line in the same panel indicates the same relation with the normalization increased by factor of 3. Just like with  $L_1$ , this line agrees well with the observed data.

$L_0$  “appears” at the same luminosity levels as when  $L_2$  “disappears”. The non-detection of  $L_0$  at low flux may be again due to the sensitive and limited frequency band of the PSDs. The  $\text{rms}_0$  remains rather constant as the outburst evolves, although at a low level of  $\sim 10\%$ . At the same time, just like  $L_1$ ,  $\nu_{\text{max},0}$  shifts to lower frequencies as the source luminosity decreases. At the lowest luminosity,  $\nu_{\text{max},0}$  would be too low to be detected in the frequency bandpass considered. This shift toward lower frequencies would be enhanced if  $L_0$  were affected by a similar discontinuity to that observed in  $L_1$  in the “frequency–time” relation at MJD 53635 (see Fig. 3). Consequently, it is possible that  $L_0$  operates at all times, and that we cannot detect it when  $\nu_{\text{max},0}$  shifts to frequencies lower than  $\sim 0.2$  Hz, when both  $L_1$  and  $L_2$  are detected in the PSDs.

Alternatively,  $L_0$  and  $L_2$  might physically disappear at lower/higher luminosities, respectively because the source changes its spectral state. This possibility is supported by the fact that the moments of appearing and disappearing of  $L_0$  and  $L_2$  coincide with distinct spectral changes (see dashed lines in Figs 1 and 3), which may indicate the onset of the “hard-soft-hard” transition. Thus  $L_2$  would appear only in the hard state, while  $L_0$  would do so in the soft-intermediate state.

### 3.3 The spectral–timing relations in GRO J1655–40

S11 fitted the hard X-ray spectrum ( $E \geq 2$  keV) of GRO J1655–40 using two different models: 1) a thermal Comptonisation model (THCOMP), and 2) a hybrid thermal/non-thermal Comptonisation model (EQPAIR) (plus a DISKBB in both cases). The spectral shape in the first case is determined by the photon index  $\Gamma$ . In the second model, it is the ratio of power in the hot electrons to that in the seed photons,  $\ell_h/\ell_s$ , that determines the shape of the spectrum. This so-called *compactness* ratio depends mainly on the geometry of the accretion flow.

We show in this work that the Lorentzian peak frequencies correlate tightly with luminosity. Since S11 showed that both  $\Gamma$  and  $\ell_h/\ell_s$  correlate with the source luminosity, we expect a strong correlation between Lorentzian peak frequencies,  $\Gamma$  and  $\ell_h/\ell_s$ , as well. This is shown in Fig. 6. Due to the fact that  $L_1$  is detected in most of the PSDs, in this figure we plot  $\Gamma$  vs  $\nu_{\text{max},1}$  (top panel) and the  $(\ell_h/\ell_s) - \nu_{\text{max},1}$  relation (bottom panel).

Both panels in Fig. 6 show that the relationship between spec-

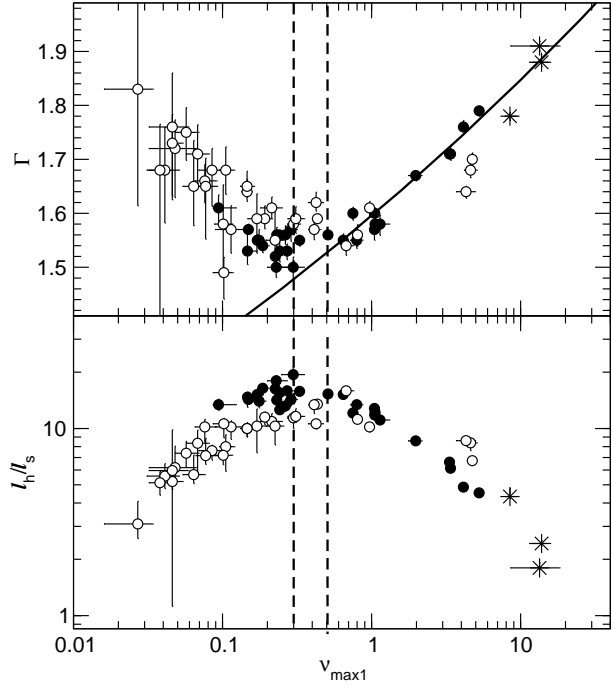


**Figure 6.** Relationship between  $\nu_{\text{max},1}$  and the spectral slope  $\Gamma$  (top panel) and the compactness ratio,  $\ell_h/\ell_s$  (bottom panel). The dashed lines indicate the range of  $\nu_{\text{max},1}$  values at which the “spectral – timing” relation in GRO J1655–40 changes. Filled/open circles indicate the rise and decay phase data. Stars represent the hard-intermediate state observations.

tral shape and  $\nu_{\text{max},1}$  is bimodal. At frequencies lower than the frequencies indicated by the dashed lines in Fig. 6 (when  $L \lesssim 0.006 - 0.01L_{\text{Edd}}$ ),  $\nu_{\text{max},1}$  anti-correlates with spectral shape: as the peak frequency increases (together with increasing flux) the spectrum hardens (i.e.  $\Gamma$  decreases) and, equivalently,  $\ell_h/\ell_s$  increases. However, at higher frequencies (i.e. luminosities) the photon index ( $\ell_h/\ell_s$ ) and peak frequency correlate positively (anti-correlate).

Note that, in both panels, we do not detect a strong “hysteresis” effect in the sense that, at frequencies higher than those indicated by the vertical dashed lines, the “spectral – timing” relation is more or less the same during the rise and decay phases of the outburst. This is mostly due to the fact that a “hysteresis” effect is also observed in both  $\Gamma$  and  $\ell_h/\ell_s$  vs  $L$  plots (cfr. Fig. 2 and Fig. 4 in S11). Because the effect follows the same direction in both spectral and timing parameters when plotted as a function of luminosity, the amplitude of the effect reduces when  $\Gamma$  or  $\ell_h/\ell_s$  are plotted against  $\nu_{\text{max},1}$ .

We used the  $(\Gamma, \nu_{\text{max},1})$  data above  $0.01L_{\text{Edd}}$  during the rise phase, and we found that the power-law relation:  $\nu_{\text{max},1} \propto \Gamma^{0.06 \pm 0.01}$ , (solid line in the top panel of Fig. 6) describe well the positive correlation between  $\nu_{\text{max},1}$  and  $\Gamma$  at high luminosities. In fact, this relation describes the correlation for both the rise and decay data sets, in agreement with the comments we made above about the weakness of the hysteresis effects in these plots.

## 4 DISCUSSION

In this work we present the results from the study of the aperiodic variability of the black-hole binary GRO J1655–40 during the 2005 outburst. We analysed the same observations as S11. They include all the observations that showed a power-law photon index



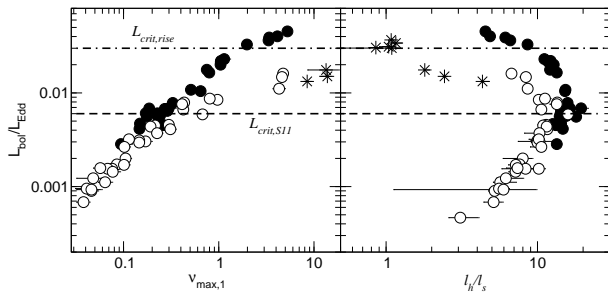


**Figure 7.** The “ $\nu_{\max,1}$ –luminosity” relation (left panel) and the “ $\ell_h/\ell_s$ –luminosity” relation (right panel) in GRO J1655–40. Filled/open circles indicate the rise and decay phase data. Stars represent the hard-intermediate state observations. The dashed and dot-dashed lines indicate the  $L_{\text{crit},S11}$  ( $\sim L_{\text{crit},\text{decay}}$ ) and  $L_{\text{crit},\text{rise}}$  luminosity levels, respectively.

below 2. In the classification scheme defined by the “hardness-intensity” diagram (see e.g. Belloni 2010), all our observations, except for those at the beginning of the decay, correspond to the canonical hard state. The first eight observations of the decay correspond to the hard-intermediate state or the transition between the two states (Motta et al. 2012). While S11 performed a spectral variability analysis of GRO J1655–40, we concentrate on its broad-band noise properties and variability. We followed an approach which is similar to that of Nowak (2000), Pottschmidt et al. (2003), and Axelsson et al. (2005) on Cyg X–1, namely, we obtained a power spectrum for each observation and fit it with a number of Lorentzian profiles. It has been shown that the multi-Lorentzian fit provides a unified description of the timing features across all kinds of accreting X-ray binaries (Belloni et al. 2002; Klein-Wolt & van der Klis 2008; Reig 2008).

We find that the power spectral density (PSD) or simply power spectra are well fitted by a combination of three broad Lorentzians ( $L_0$ ,  $L_1$  and  $L_2$ ) and a QPO, which we did not consider. At the highest flux, the PSDs are well fitted by a single Lorentzian ( $L_0$ ). At all other cases, the PSDs are well fitted by the sum of two Lorentzians, either  $L_0$  and  $L_1$  (at high flux), or  $L_1$  and  $L_2$  (at low flux). The whole PSD depends strongly on the source luminosity: it shifts to higher frequencies, as the luminosity increases during the rise phase of the outburst, and then shifts back to lower frequencies as the luminosity decreases during the decay phase, in agreement with what is observed in other black-hole binaries.

Our first main result is the detection of a strong “hysteresis” effect:  $\nu_{\max,0,\text{decay}}$  and  $\nu_{\max,1,\text{decay}}$  are always higher than  $\nu_{\max,0,\text{rise}}$  and  $\nu_{\max,1,\text{rise}}$ , as long as the source luminosity is greater than  $L_{\text{crit},S11}$ . Hysteresis is a well-known effect observed in the spectral parameters (i.e., photon index, X-ray colours, iron line strength) of transient (Homan et al. 2001; Nowak et al. 2002; Dunn et al. 2008) and persistent (Smith et al. 2007) black-hole binaries, and neutron-star binaries (Maccarone & Coppi 2003). Most remarkable is the hysteresis observed in the X-ray colours that gives rise to the characteristic  $q$ -shape of the hardness-intensity diagram of black-hole transients (Belloni et al. 2005). A hysteresis effect between the root mean square (rms) amplitude of the variability and the net count-rate has also been reported (Muñoz-Darias et al. 2011). Even the near-IR flux seems to show a hysteresis effect in black-hole state transitions (Russell et al. 2007). In this work we show that hystere-

sis is also present in the evolution of the Lorentzian peak frequencies during the outburst of GRO J1655–40<sup>2</sup>.

Our second major result is that, just like the spectral properties of the source, the hard state timing properties of GRO J1655–40 also change above/below a “critical” luminosity level. However, we also find that this level is different during the rise and the decay phase of the outburst:  $L_{\text{crit},\text{rise}} \sim 0.03L_{\text{Edd}}$ , while  $L_{\text{crit},\text{decay}} \sim L_{\text{crit},S11} \sim 0.006L_{\text{Edd}}$ . Fig. 7 shows the “ $L_1$  peak frequency – luminosity” diagram (based on the results presented in this work; left panel), and the “ $\ell_h/\ell_s$  – luminosity” diagram (using the S11 results; right panel). The dot-dashed and dashed lines indicate the  $L_{\text{crit},\text{rise}}$  and  $L_{\text{crit},S11}$  levels, respectively. The hysteresis effect is evident in both plots, but the details differ. Both the rise and the decay “spectral – luminosity” relation change around  $L_{\text{crit},S11}$ . At luminosities greater than  $L_{\text{crit},S11}$ , the rise and decay data follow two *different* paths. Moreover, the “ $L_1$  peak frequency – luminosity” relation changes above  $L_{\text{crit},\text{rise}}$  (and not  $L_{\text{crit},S11}$ ) during the rise phase. However, the data above the critical levels are characterised by a similar slope (i.e.  $\nu_{\max,1} \propto (L_{\text{bol}}/L_{\text{Edd}})^4$ ) during both the rise and the decay phases.

At lower luminosity, below  $L_{\text{crit},S11}$ , we observe the same “peak frequency – luminosity” relation for both the rise and decay phases. Note that the “ $\ell_h/\ell_s$  – luminosity” diagram is analogous to the traditional  $q$ -shaped “hardness-intensity” diagram, where X-ray colours have been replaced by the ratio  $\ell_h/\ell_s$  and the count rate by luminosity (compare the right panel in Fig. 7 with the top panel in Fig. 1 in Motta et al. 2012). The luminosity level  $L_{\text{crit},S11}$  corresponds to a 3–20 keV count rate of PCU2  $\sim 50$  count  $\text{s}^{-1}$ , which is the count rate below which colours and variability levels (rms) follow also the same trend. The “hardness-intensity” diagram (Fig. 1 in Motta et al. 2012), together with Figs 6 and 7 illustrate the common behaviour of the spectral, timing and colour parameters below  $L_{\text{crit},S11}$ , irrespective of whether the source is in the rise or decay of the outburst.

A model that is frequently assumed to explain the X-ray properties of BHBs during their outbursts is the so called “truncation disc” model. According to this model, the standard cool, optically thick, geometrically thin accretion disc (Shakura & Sunyaev 1973) is truncated at some radius,  $R_{\text{trunc}}$ , which is greater than the radius of the innermost stable circular orbit radius,  $R_{\text{in}}$ . A hot, optically thin, geometrically thick accretion flow (usually referred to as the “corona”) is assumed to extend from  $R_{\text{trunc}}$  to  $R_{\text{in}}$ . A fraction of the disc photons are incident on the hot flow where they are Compton-up-scattered by the hot electrons, giving rise to the hard X-ray, power-law like component in the X-ray spectra.

As the source luminosity increases/decreases during the rise/decay phase of the outburst,  $R_{\text{trunc}}$  is believed to decrease/increase, respectively. If the Lorentzian frequencies correspond to a characteristic time scale at  $R_{\text{trunc}}$  (i.e. at the outer radius of the corona), it is natural to expect that the PSDs will also shift to higher/lower frequencies during the rise/decay phase of the outburst, as observed. If this is the case, the hysteresis effect we observe suggests that, whatever the truncation physical mechanism may be, it may *not* operate at the same rate with luminosity: at the *same* luminosity level,  $R_{\text{trunc},\text{rise}} > R_{\text{trunc},\text{decay}}$  (as long as  $L > L_{\text{crit},S11}$ ).

The  $\nu_{\max,1}$  may be identified with the viscous time scale at

<sup>2</sup> Some evidence for a hysteresis pattern associated with a broad-band component can be seen in Fig. 7 of Belloni et al. (2005), although these authors do not discuss the implications of such result.

$R_{trunc}$ , which should modulate the propagation of fluctuations in mass accretion rate within the hot flow. Recent calculations of the viscous frequency,  $\nu_{visc}$ , as a function of radius in a BH binary predict values of the order of  $\sim 3 \times 10^{-2} - 10$  Hz, when  $50R_g \geq R_{trunc} \geq 5 - 8R_g$  (see the green and red lines in the middle panel of Fig. 1 in Ingram & Done 2012), where  $R_g$  is the gravitational radius of the BH. This is very similar to the range of  $\nu_{max,1}$  values we observe in GRO J1655–40. Interestingly, the same authors show that, in the case of tilted accretion flows, the “ $\nu_{visc}$ –radius” relation should steepen considerably at radii smaller than the so-called “bending wave radius”,  $R_{bw}$ , which is expected from a misaligned flow. Consequently, if  $\nu_{max,1} \sim \nu_{visc}(R_{trunc})$ , and  $R_{trunc}$  decreases with increasing source luminosity, then a steepening of the “ $\nu_{max,1} - (L_{bol}/L_{Edd})$ ” relation (identical during the rise and decay phase) should appear when  $R_{trunc}$  becomes smaller than  $R_{bw}$ . The “critical” luminosity levels should correspond to the source luminosity when  $R_{trunc} < R_{bw}$ , and since  $L_{crit,rise} \neq L_{crit,decay}$ ,  $R_{trunc}$  should become smaller than  $R_{bw}$  at different luminosity levels during the rise and decay phases.

Another possibility though is that the “ $R_{trunc}$ –luminosity” relation is the same during both the rise and decay phases, but the bending wave radius in the decay phase is greater than  $R_{bw}$  in the rise phase. In this case, the steep  $\nu_{visc} - R_{trunc}$  relation in the decay phase will last until lower luminosities, hence  $L_{crit,decay} < L_{crit,rise}$ , as observed. At the same time, since  $\nu_{visc}$  depends on  $R_{bw}$  (see equation 2 in Ingram & Done 2012), this scenario may also explain the difference we observe in the normalization of the  $\nu_{max,1} - L_{bol}/L_{Edd}$  relation in the rise and decay phases. Nevertheless, even in this case, since  $R_{bw}$  depends on the ratio of the height of the flow over its radius, our results indicate that the evolution of the disc/coronal parameters with luminosity should not be the same during the rise and decay phase of the outburst.

The coronal emission may also vary due to magneto-acoustic waves propagating within the hot flow. Cabanac et al. (2010) have investigated the timing properties of the hot corona in the case when an external excitation propagates radially within the corona at the sound speed. They showed that in this case, the filtering effect of the corona leads to the appearance of broad-band noise components in the PSDs, which are well fitted by zero-centered Lorentzians. The peak frequencies of these Lorentzians should scale as  $\sim 2.5 \times 2\pi c_s/r_j$ , where  $r_j$  is the outer radius of the corona, and  $c_s$  is the sound speed. In the case of a 10 solar mass BH, a hot corona of a temperature  $\sim 100$  keV, and  $50R_g \geq r_j = R_{trunc} \geq 10R_g$ , the Lorentzian peak frequencies should range between  $\sim 1.7 - 8.5$  Hz, which is almost identical to the observed range of  $\nu_{max,2}$ .

S11 observed that the “spectral shape – luminosity” relation in GRO J1655–40 changes when  $L \sim 0.006L_{Edd}$ : at lower (higher) luminosities  $\Gamma$  and  $L_{bol}/L_{Edd}$  anti-correlate (correlate positively). Within the “truncation disc” model, they interpreted this result as an evidence for a change in the X-ray radiation mechanism, whereby the seed photons that feed the Compton process have a different origin depending on luminosity. At luminosities less than  $\sim 0.01L_{Edd}$ , the seed photons may come from the cyclo-synchrotron radiation of the hot flow itself. Above the “critical” luminosity limit, the seed photons could stem from the thermal emission of the truncated disc. Within the truncation disc model, and following S11’s interpretation, the fact that  $L_0$  is detected when  $L > L_{crit,S11}$  (both during the rise and the decay phase of the outbursts) may suggest that  $L_0$  is associated with variability processes of the accretion disc seed soft photons. The seed photon flux may vary on the viscous time scale (of the disc) at  $R_{trunc}$ , and could induce a variation in the output of the hot corona. If what we see is actually the Comp-

tonized radiation (not the disc), even at this relatively high luminosity, then the small rms amplitude exhibited by  $L_0$  can be explained because the temperature of the corona can adjust very quickly to the changes of soft photon flux from the disc. In this case, the fluctuations are damped, i.e. huge fluctuation of soft seed photons flux leads to modest change in Comptonized flux (Malzac & Jourdain 2000). This would also be consistent with the interpretation of S11: at luminosities  $< 0.01L_{Edd}$  synchrotron seed photons dominate over disc photons and the disc variability cannot be seen anymore in the Comptonized radiation. On the other hand, if the radiation at  $L > L_{crit,S11}$  came from the disc, then we would conclude that the disc is not varying significantly when the source luminosity is high.

Finally, the “spectral – timing” correlations we observe between the Lorentzian peak frequencies and the hard X-ray spectral slope should be a by-product of the individual relations between  $\nu_{max}$  and  $\Gamma$  with  $(L_{bol}/L_{Edd})$  that are reported in this work and in S11. Interestingly, the  $\nu_{max} \propto \Gamma^{0.06}$  relation that we observe above  $L_{crit}$  is identical to a similar relation reported by Papadakis et al. (2009) for a few, bright AGN. This is one more evidence for the similarity between the spectral and variability properties of BHBs and AGN. In addition, this result reinforces the interpretation of Papadakis et al. (2009) that this relation in AGN is due to the fact that both the characteristic frequencies and the average spectral slope do depend on the source luminosity (and ultimately on accretion rate), hence the presence of this relation in AGN, just like in GRO J1655–40 when the source luminosity exceeds the “critical” level of  $\sim 0.01$  of the Eddington limit.

## 5 SUMMARY AND CONCLUSION

We have studied the aperiodic variability of the black-hole binary GRO J1655–40 at the beginning and end of its 2005 outburst. We found that, just like with its spectral evolution, the variability evolution of the broad-band noise components in the power spectrum with luminosity follows the same trend for both the rise and decay data, as long as the source luminosity is smaller than  $\sim 0.006$  of the Eddington limit. At higher luminosities, the evolution of the broad-band noise with luminosity is different during the rise and decay phases, and a strong hysteresis pattern appears. Our results can be summarised as follows:

*The PSD evolution during the rise phase.* 1)  $L \leq L_{crit,rise}$ : The PSDs are well described by the sum of  $L_1$  and  $L_2$ . Both  $\nu_{max,1}$  and  $\nu_{max,2}$  shift to higher frequencies as the source luminosity increases:  $\nu_{max,1} \propto (L_{bol}/L_{Edd})$  and  $\nu_{max,2} \propto (L_{bol}/L_{Edd})^{0.57}$ . 2)  $L \geq L_{crit,rise}$ : The  $L_1$  rms starts decreasing with source flux, and  $\nu_{max,1} \propto (L_{bol}/L_{Edd})^4$ .  $L_2$  is not detected anymore, while  $L_0$  appears. Its peak frequency also increases with increasing luminosity according to the relation:  $\nu_{max,0} \propto (L_{bol}/L_{Edd})^{5.1}$ .

*The PSD evolution during the decay phase.* 1)  $L \geq L_{crit,decay}$ : The PSDs are well fitted mainly by the sum of  $L_0$  and  $L_1$ . As the luminosity decreases,  $\nu_{max,0}$  and  $\nu_{max,1}$  also decrease. We find that  $\nu_{max,1} \propto (L_{bol}/L_{Edd})^4$ , and  $\nu_{max,0} \propto (L_{bol}/L_{Edd})^{5.1}$ , similarly to what we observe in the rise phase, when  $L > L_{crit,rise}$ . The only difference is that the  $\nu_{max} - L$  relations have a normalization which is  $\sim 3$  times smaller than before. 2)  $L \leq L_{crit,decay}$ : The  $L_1$  and  $L_2$  peak frequencies shift to lower frequencies as the luminosity decreases, in a fashion similar to the rise phase, when the source luminosity was smaller than  $L_{crit,rise}$ .

We attempt to explain our results within the truncation disc model and conclude that each broad-band noise component may be attributed to a different process in the accretion disc: variability

processes associated with the seed photon flux ( $L_0$ ), viscous time scales at the truncation radius ( $L_1$ ), and magneto-acoustic waves propagating in the accretion flow ( $L_2$ ). Irrespective though of the physical identification of the Lorentzian peak frequencies, our results strongly suggest that, if the truncation disc/corona model is valid, the evolution of the disc/coronal properties with luminosity cannot be the same during the rise and decay phases of the outburst.”

## ACKNOWLEDGMENTS

JM acknowledges financial support from the French Research National Agency: CHAOS project ANR-12-BS05-0009 (<http://www.chaos-project.fr>) and from PNHE in France.

## REFERENCES

- Axelsson, M., Borgonovo, L., & Larsson, S., 2005, *A&A*, 438, 999
- Belloni, T., Psaltis, D., & van der Klis, M., 2002, *ApJ*, 572, 392
- Belloni, T., Homan, J., Casella, P., van der Klis, M., Nespoli, E., Lewin, W. H. G., Miller, J. M., & Mndez, M., 2005, *A&A*, 440, 207
- Belloni, T., 2010, *LNP*, 794, 53
- Cabanac, C., Henri, G., Petrucci, P.-O., Malzac, J., Ferreira, J., & Belloni, T. M., 2010, *MNRAS*, 404, 738
- Casella, P., Belloni, T., & Stella, L., 2005, *ApJ*, 629, 403
- Chakrabarti, S. K., Debnath, D., Nandi, A., & Pal, P. S., 2008, *A&A*, 489, L41
- Cowley, A. P., Crampton, D., Hutchings, J. B., Remillard, R., & Penfold, J. E., 1983, *ApJ*, 272, 118
- Debnath, D., Chakrabarti, S. K., Nandi, A., & Mandal, S., 2008, *BASI*, 36, 151
- Dunn, R. J. H., Fender, R. P., Körding, E. G., Cabanac, C., & Belloni, T., 2008, *MNRAS*, 387, 545
- Foellmi, C., Depagne, E., Dall, T.H., & Mirabel, I.F., 2006, *A&A*, 2006, 457, 249
- Gallo, E., Homan, J., Jonker, Peter G., & Tomsick, J. A., 2008, *ApJ*, 683, L51
- Gierliński, M., Maciolek-Niedźwiecki, A., & Ebisawa, K., 2001, *MNRAS*, 325, 1253
- Hjellming, R. M., & Rupen, M. P., 1995, *Nature*, 375, 464
- Homan, J., Wijnands, R., van der Klis, M., Belloni, T., van Paradijs, J., Klein-Wolt, M., Fender, R., & Méndez, M., 2001, *pJS*, 132, 377
- Ingram, A., & Done, C., 2012, *MNRAS*, 419, 2369
- Jahoda, K., Swank, J.H., Giles, A.B., Stark, M.J., Strohmayer, T., Zhang, W., & Morgan, E.H., 1996, *SPIE*, 2808, 59
- Klein-Wolt, M., & van der Klis, M., 2008, *ApJ*, 675, 1407
- Kylafis, N. D., Papadakis, I. E., Reig, P., Giannios, D., & Pooley, G. G., 2008, *A&A*, 489, 481
- Maccarone, T. J., & Coppi, P. S. 2003, *MNRAS*, 338, 189
- Malzac, J., & Jourdain, E., 2000, *A&A*, 359, 843
- Markoff, S., Nowak, M. A., & Wilms, J., 2005, *ApJ*, 635, 1203
- Motta, S., Homan, J., Muñoz Darias, T., Casella, P., Belloni, T. M., Hiemstra, B., & Méndez, M., 2012, *MNRAS*, 427, 595
- Muñoz-Darias, T., Motta, S., & Belloni, T. M., 2011, *MNRAS*, 410, 679
- Nandi, A., Debnath, D., Mandal, S., & Chakrabarti, S. K., 2012, *A&A*, 542, A56
- Nowak, M. A., Vaughan, B. A., Wilms, J., Dove, J. B., Begelman, M. C., 1999, *ApJ*, 510, 874
- Nowak, M. A., 2000, *MNRAS*, 318, 361
- Nowak, M. A., Wilms, J., Dove, J. B., 2002, *MNRAS*, 332, 856
- Orosz, J. A., & Bailyn, C. D., 1997, *ApJ*, 477, 876
- Papadakis, I. E., Sobolewska, M., Arevalo, P., Markowitz, A., McHardy, I. M., Miller, L., Reeves, J. N., & Turner, T. J., 2009, *A&A*, 494, 905
- Pottschmidt, K., Wilms, J., Nowak, M. A., Pooley, G. G., Gleissner, T., Heindl, W. A., Smith, D. M., Remillard, R., & Staubert, R., 2003, *A&A*, 407, 1039
- Press, W. H., Teukolsky, S. A., Vetterling, W. T., & Flannery, B. P., 1992, in *Numerical Recipes: The art of scientific computing*, Cambridge University Press.
- Reig, P., 2008, *A&A*, 489, 725
- Remillard, R. A., & McClintock, J. E., 2006, *ARA&A*, 44, 49
- Russell, D. M., Maccarone, T. J., Körding, E. G., & Homan, J., 2007, *MNRAS*, 379, 1401
- Shakura, N. I. & Sunyaev, R. A., 1973, *A&A*, 24, 337
- Shaposhnikov, N., Swank, J., Shrader, C. R., Rupen, M., Beckmann, V., Markwardt, C. B., & Smith, D. A., 2007, *ApJ*, 655, 434
- Shaposhnikov, N. & Titarchuk, L., 2009, *ApJ*, 699, 453
- Smith, D.M., Dawson, D.M., & Swank, J.H., 2007, *ApJ*, 669, 1138
- Sobolewska, M. A., Gierliński, M., & Siemiginowska, A., 2009, *MNRAS*, 394, 1640
- Sobolewska, M. A., Papadakis, I. E., Done, C., & Malzac, J., 2011, *MNRAS*, 417, 280
- Webster, B. L., & Murdin, P., 1972, *Nature*, 235, 37
- Wu, Q., & Gu, M., 2008, *ApJ*, 682, 212
- Zhang, S.N., Wilson, C.A., Harmon, B. A., Fishman, G. J., Wilson, R. B., Paciesas, W. S., Scott, M., & Rubin, B. C., 1994, *IAUC* 6046